RSC Advances

PAPER

View Article Online
View Journal | View Issue

Check for updates

Cite this: RSC Adv., 2026, 16, 2652

DMF-mediated synthesis of N,S-co-doped carbon quantum dots and their fluorescence quenching mechanism toward Hg^{2+} *via* surface complexation

Yongjian Pan,[a] Shancai Guo,[a] Teng Wang,[a] Jianyuan Lin,*[a] Zhijian Jia,[b] Fuhang Xu,[a] Renyue Huang,[a] Haili Wang,[a] Chunjie Bai[a] and Jianghua Chen[c]

Received 3rd November 2025
Accepted 1st January 2026

DOI: 10.1039/d5ra08448b

rsc.li/rsc-advances

Nitrogen and sulfur co-doped carbon quantum dots (N,S-CQDs) were synthesized *via* a green, one-step hydrothermal method using waste lemon peel as the carbon source and glutathione (GSH) as the N,S dopant in a dimethylformamide (DMF) medium. The reaction was conducted at 180 °C for 10 hours to achieve efficient synthesis. The resulting N,S-CQDs showed excellent water dispersibility, strong photostability, and bright fluorescence, with optimal excitation and emission wavelengths of 340 nm and 420 nm, respectively. High-resolution transmission electron microscopy (HRTEM), X-ray photoelectron spectroscopy (XPS), and Fourier transform infrared spectroscopy (FT-IR) confirmed their uniform morphology and successful incorporation of nitrogen and sulfur heteroatoms. Notably, the fluorescence of the N,S-CQDs could be rapidly and selectively quenched by Hg^{2+} within 10 minutes at room temperature, without requiring any additional surface modification of the CQDs or auxiliary reagents in the sensing procedure. Under optimized conditions, the sensor exhibited a linear fluorescence quenching response to Hg^{2+} over the concentration range of 17.6 nM to 20 μM ($R^2 = 0.9899$), with a low detection limit of 17.6 nM. Mechanistic studies suggested that the quenching primarily resulted from the formation of nonfluorescent complexes between Hg^{2+} and functional groups on the CQD surface. The developed sensor was successfully applied to detect trace levels of Hg^{2+} in real lake water samples collected near textile manufacturing sites, demonstrating its potential as a sustainable, rapid, and cost-effective tool for practical environmental mercury monitoring.

1 Introduction

Mercury (Hg) is a highly toxic heavy metal that is widely used in the chemical,[1] electronic, pharmaceutical, and coal[2] combustion industries.[3,4] Both inorganic mercury and organic methylmercury can easily accumulate in the environment and become magnified through the food chain.[5,6] As a result, mercury contamination poses a serious threat to ecosystems and human health. Studies have shown that more than half of inorganic mercury is discharged into water bodies through industrial wastewater, mining emissions, and atmospheric deposition.[7] It can persist in non-degradable forms in rivers, lakes, groundwater, and municipal wastewater.[8] Mercury ions are highly electrophilic and readily bind to thiol groups in living organisms. This interaction can disrupt neurological and immune system functions, and even low doses may cause cognitive impairment and kidney damage.[9,10] Therefore, it is important to develop *in situ* detection technologies for Hg^{2+} that offer high sensitivity, high selectivity, low cost, non-toxicity, and a fast response. Such methods are essential for effective environmental monitoring and risk assessment.

Although traditional mercury ion detection techniques, such as atomic absorption spectrometry (AAS),[11] inductively coupled plasma mass spectrometry (ICP-MS),[12] and electrochemical sensing,[13] offer excellent sensitivity and accuracy, they have several limitations. These methods often require expensive instruments, complex sample preparation, and specialized operation, which make rapid on-site detection difficult. In recent years, carbon quantum dots (CQDs) have emerged as promising fluorescent nanomaterials owing to their excellent photostability, tunable emission, low toxicity, and facile surface functionalization. Notably, heteroatom-doped CQDs, particularly nitrogen- and sulfur-co-doped CQDs (N,S-CQDs), have attracted increasing attention for Hg^{2+} sensing. Concurrently, growing emphasis has been placed on green and sustainable strategies for functional nanomaterial synthesis, especially those based on biomass-derived precursors and environmentally responsible design principles. For example, recent studies have demonstrated various

[a]Zhejiang Wanli University, Ningbo, 315100, PR China. E-mail: linjianyuan33@163.com; 365423087@qq.com; 13738675044@163.com; 18758303073@163.com; renyue_huang@163.com; 147933589@qq.com; 357796845@qq.com; 71928316@qq.com

[b]School of Materials and Chemical Engineering, Ningbo University of Technology, Ningbo, 315211, PR China. E-mail: zhijian.jia@nbut.edu.cn

[c]Ningbo Academy of Agricultural Sciences/Ningbo Key laboratory of Quality and Safety Testing and Control of Ningbo Characteristic Agricultural Products, Ningbo, 315040, PR China

green and sustainable approaches for nanomaterial synthesis, including biomass-derived carbonaceous materials, low-energy synthetic routes, and environmentally benign reaction media, providing important design principles for eco-friendly functional materials.[14–18] From a mechanistic perspective, sulfur-containing functional groups act as soft bases and exhibit strong coordination affinity toward Hg^{2+}, a typical soft acid, making S-rich CQDs intrinsically favorable platforms for selective Hg^{2+} recognition and fluorescence modulation. Beyond solution-based fluorescent probes, rational compositional and structural design has also been demonstrated as an effective strategy to enhance emission efficiency in solid-state luminescent materials, such as force-responsive or field-assisted systems, underscoring the general importance of emission regulation in advanced sensing and smart applications.[19]

Numerous studies have demonstrated the feasibility of N,S-CQDs for Hg^{2+} detection through various fluorescence mechanisms.[20] For example, Wahyudi *et al.*[21] reported an N,S-co-doped carbon dot-silver nanoparticle composite that enabled ultrasensitive "off–on" fluorescence detection of Hg^{2+} through Ag/Hg amalgam formation, achieving a detection limit of 10 nM, albeit with a multicomponent sensing architecture. Aladesuyi *et al.*[22] synthesized green-emissive N,S-co-doped carbon quantum dots *via* a one-step hydrothermal route, which enabled selective Hg^{2+} detection through static fluorescence quenching with a detection limit of 28.9 nM and was successfully applied to seafood analysis. Qi *et al.*[23] synthesized nitrogen and sulfur co-doped carbon dots (NS-CDs) by a thermal cracking method, using taurine and citric acid as precursors. The resulting NS-CDs had a high quantum yield of 68.94%. These NS-CDs were used as a fluorescent sensor for the integrated detection of Hg^{2+} and glutathione (GSH) based on an "on–off–off–off–on" strategy. The sensor was successfully applied to the detection of Hg^{2+} and GSH in real samples, including tap water and fetal bovine serum, and showed good reversibility. Dewangan *et al.*[24] synthesized N-CQDs as well as Ag- and Ce-co-doped CQDs *via* a hydrothermal method, achieving enhanced quantum yields and enabling an "off–on" fluorescence sensing strategy for Hg^{2+} and captopril, with detection limits as low as 0.93 nM for Hg^{2+} and 0.46 μM for captopril, and good performance in real samples. Despite these advances, most reported systems still suffer from one or more limitations, such as multistep or energy-intensive synthesis, reliance on auxiliary nanocomponents, limited sulfur accessibility, or insufficient consideration of sustainability and green chemistry principles. These factors restrict their large-scale production and practical deployment for *in situ* environmental monitoring.

In this work, we report a green and efficient DMF-mediated one-step solvothermal strategy for the synthesis of N,S-co-doped carbon quantum dots using waste lemon peels as a renewable carbon source and glutathione (GSH) as a nitrogen–sulfur co-dopant. The use of DMF facilitates efficient heteroatom incorporation and promotes the formation of sulfur-rich surface states, providing abundant Hg^{2+}-binding sites. The resulting N,S-CQDs exhibit strong fluorescence, excellent aqueous stability, and high selectivity toward Hg^{2+} through Hg–S coordination-induced fluorescence quenching. Compared with previously reported N,S-doped CQDs,[25] this approach enables simplified synthesis, enhanced sulfur retention and surface accessibility, improved Hg^{2+} selectivity through abundant soft-base sulfur sites, and competitive sensing performance, while simultaneously offering a value-added and sustainable utilization route for biomass waste.

2 Experimental

2.1 Reagents and materials

Lemons were purchased fresh from a local market, thoroughly rinsed with deionized water, air-dried, and finely ground into powder using a laboratory grinder prior to use; glutathione, *N*,*N*-dimethylformamide (DMF), silver nitrate, tetracycline, levofloxacin, ampicillin, and ciprofloxacin were purchased from Shanghai Aladdin Biochemical Technology Co., Ltd. Fourier-transform infrared (FT-IR) spectra were obtained using a Vertex 70 spectrometer. UV-vis absorption spectra were recorded on a UV-3000PC spectrophotometer provided by Zhejiang Wanli University, and fluorescence spectra were measured using a Hitachi F-4600 fluorescence spectrophotometer.

2.2 Preparation and condition optimization of N,S-CQDs

N,S-CQDs were synthesized *via* a simple one-step solvothermal method. First, 0.6 g of finely ground lemon peel was dispersed in 10 mL of dimethylformamide (DMF). Next, 0.2 g of reduced glutathione (GSH) was added, and the mixture was ultrasonicated at room temperature for 30 min. The resulting suspension was transferred to a 50 mL Teflon-lined stainless-steel autoclave and heated at 180 °C for 10 h. After cooling to room temperature, the reaction mixture was centrifuged at 8000 rpm for 10 min, and the supernatant was filtered through a 0.22 μM membrane to yield a brown–green N,S-CQDs solution. This solution was stored at 4 °C. Under 370 nm UV excitation, the N,S-CQDs emitted bright blue fluorescence. DMF was selected as the reaction medium due to its strong solvating ability and high boiling point, which facilitate efficient carbonization and heteroatom incorporation. Although DMF is not considered a green solvent, its use in this study was limited to small volumes, and future work will explore more environmentally benign alternatives.

To further optimize the preparation conditions of N,S-CQDs and their performance in target ion detection, the effects of key parameters were investigated. These included synthesis temperature (120–200 °C), heating time (6–12 h), amount of glutathione added, pH of the reaction system, as well as response time and temperature during the detection process. The impact of these factors on fluorescence performance and detection sensitivity was systematically studied. The fluorescence response of N,S-CQDs to Hg^{2+} was used as the main evaluation index. By adjusting the above parameters, the optimal synthesis and detection conditions were determined to maximize the fluorescence quantum yield and sensitivity.

2.3 Standardized procedure for Hg^{2+} detection using N,S-CQDs

The N,S-CQDs solution was diluted 50-fold with purified water and set aside. For each test, 2.5 mL of the diluted N,S-CQDs solution and 2.5 mL of the Hg^{2+} solution at various concentrations were added to a 5 mL centrifuge tube. The mixture was thoroughly mixed and incubated at room temperature for 10 minutes. After incubation, 1 mL of the reaction mixture was collected, and the fluorescence spectra were recorded using a Hitachi F-4600 fluorescence spectrophotometer. The measurement parameters were set as follows: excitation wavelength at 370 nm, emission spectra recorded from 300 to 700 nm, excitation and emission slit widths at 10 nm, and a scanning speed of 1200 nm min^{-1}. Each concentration was measured in triplicate, and the average fluorescence intensity was used for analysis. The changes in fluorescence intensity at different Hg^{2+} concentrations were compared to evaluate the detection sensitivity and linear response range of the N,S-CQDs probe for Hg^{2+}.

2.4 Selectivity and sensitivity for Hg^{2+} detection

To evaluate the selectivity and anti-interference capability of the N,S-CQDs for Hg^{2+} detection, a series of interference experiments were conducted. Common metal ions, including Al^{3+}, Ba^{2+}, Ca^{2+}, Cd^{2+}, Cu^{2+}, Fe^{2+}, Fe^{3+}, K^+, Mg^{2+}, Mn^{2+}, Na^+, and Zn^{2+}, were tested for their potential interfering effects. The potential interference of four commonly used antibiotics—tetracycline (TC), levofloxacin (LEV), ampicillin (AMP), and ciprofloxacin (CIP)—on Hg^{2+} detection was also investigated. In these experiments, each interferent was first prepared as a 1 mM stock solution in distilled water. The stock solutions were then diluted to the required concentrations and tested for their fluorescence response. This approach was used to assess the sensitivity and anti-interference performance of the N,S-CQDs probe for Hg^{2+} detection.

2.5 Application of N,S-CQDs for detecting Hg^{2+} in real water samples

To validate the practical utility of the synthesized N,S-CQDs fluorescent probes for detecting Hg^{2+} in real water environments, spiked recovery experiments were performed using water samples collected from Lake Water Adjacent to Textile Factories. During the experiment, the collected lake water samples were first centrifuged at 8000 rpm for 10 minutes and then filtered through a 0.22 μm membrane to remove particulate impurities. Different concentrations of Hg^{2+} standard solutions were then added to the treated samples. The fluorescence responses were measured according to the standard N,S-CQDs detection procedure described above, in order to evaluate the probes' performance and reliability in actual complex water environments.

3 Results and discussion

3.1 Structural characterization of N,S-CQDs

The morphology of the prepared N,S-CQDs was characterized by transmission electron microscopy. As shown in Fig. 1(a), the N,S-CQDs are uniformly dispersed on the substrate and exhibit a nearly spherical morphology with a uniform size distribution. No obvious agglomeration is observed, and the average diameter is approximately 2.45 nm. The overall background displays slight amorphous carbon or organic residues, which do not affect the observation of individual particles. Fig. 1(b) clearly shows lattice fringes with spacings of 0.21 nm and 0.23 nm, which are attributed to the (100) planes of the short-range ordered microcrystalline structure of graphitic carbon.[26–28] In addition, local lattice distortions and bends indicate defect sites introduced by nitrogen and sulfur doping. These defects help modulate the electronic structure and enhance the fluorescence properties of the N,S-CQDs.

FT-IR analysis showed a broad absorption peak at 3400 cm^{-1}, corresponding to the O–H and N–H stretching vibrations. This indicates that the surface of the CQDs is rich in hydroxyl and amine groups. The moderate-intensity peak at 2950–2850 cm^{-1} is attributed to the C–H stretching vibrations of $-CH_2-$ and $-CH_3$ groups, which likely originate from polysaccharide residues or organic side chains in the lemon peel. The distinct and strong peaks at 1720–1700 cm^{-1} correspond to the C=O stretching vibrations of ester and carboxyl groups derived from the lemon peel. The medium-intensity absorption at 1650–1600 cm^{-1} is assigned to C=C backbone vibrations and amide I bands (N–H bending and C–N stretching). This reflects the presence of aryl or heterocyclic structures formed during carbonization, as well as residual amide groups from GSH. The absorption at 1400–1380 cm^{-1}, corresponding to $-CH_2$ bending and $-COO^-$ symmetric stretching, suggests the presence of polysaccharide or protein-like moieties. The vibrational peaks at 1250–1200 cm^{-1} and 1100–1050 cm^{-1} correspond to C–N or C–O–C stretching vibrations, indicating the presence of amine or ether bonds and alcohol or ester C–O stretching, respectively. The fingerprint region at 800–600 cm^{-1} displays several weak peaks, which may be attributed to C–H out-of-plane bending and aryl ring substitution vibrations. The FT-IR spectrum confirms that GSH, lemon peel polysaccharides, and DMF interact during hydrothermal carbonization to form N,S-CQDs. These CQDs possess a core sp^2 carbon skeleton and are encapsulated by various oxygen- and nitrogen-containing functional groups, including hydroxyl, amine, amide, and carboxyl or ether bonds. The abundant surface functional groups not only enhance the water dispersibility and biocompatibility of the particles, but also provide active sites for the specific binding of metal ions or biomolecules during fluorescence sensing. Meanwhile, the conjugated C=C and C=O vibrations at 1650 cm^{-1} and 1720 cm^{-1} indicate the presence of a conjugated system consisting of heterocyclic and amide backbones.[29,30] This structure favors light absorption and fluorescence emission of the N,S-CQDs in the UV-visible region. Overall, these spectral features closely match the structures of the precursors, confirming the successful synthesis of N,S-CQDs and their potential for sensing applications.

3.2 Investigation of the optical properties of N,S-CQDs

As shown in Fig. 2, the full-scan X-ray photoelectron spectroscopy (XPS) spectrum of the N,S-CQDs reveals that their surfaces are primarily composed of carbon (C), nitrogen (N), oxygen (O), and sulfur (S) elements. Although adventitious carbon

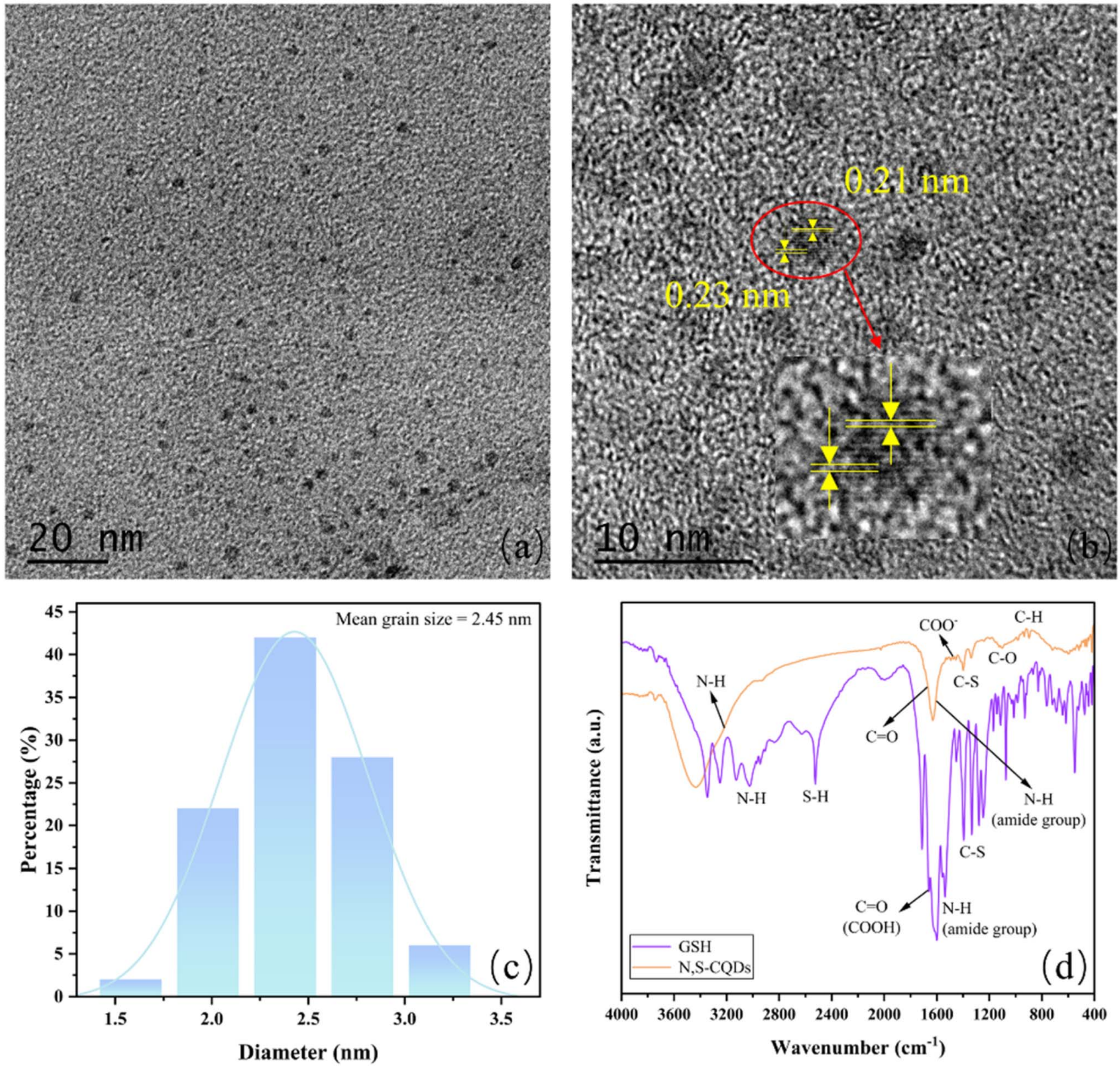

Fig. 1 (a) TEM image of the prepared N,S-CQDs. (b) High-resolution lattice fringes of N,S-CQDs. (c) Distribution of particle size for N,S-CQDs. (d) FT-IR spectra of N,S-CQDs, showing characteristic functional groups on the surface.

contamination is commonly encountered in XPS measurements, the carbon-related signals observed here are attributed to the intrinsic carbon framework of the N,S-CQDs rather than surface contamination. This conclusion is supported by the concurrent detection of chemically meaningful N 1s and S 2p signals, the well-resolved and chemically assignable C 1s components, and the strong consistency between XPS results and FT-IR analysis, which together confirm the intrinsic surface chemistry of the synthesized CQDs. The high-resolution C1s spectrum (Fig. 3(a)) can be deconvoluted into three peaks. The dominant peak at 284.67 eV is attributed to C–C/C═C bonds, corresponding to the graphitized carbon skeleton that stabilizes the electronic structure of the CQDs.[31] These groups enhance aqueous dispersibility and provide ligand sites for Hg^{2+}. The peak at 286.04 eV is assigned to C–O and C–N bonds, indicating the presence of hydrophilic functional groups such as hydroxyl, ether, and amine moieties on the surface. These functional groups improve aqueous dispersibility and introduce surface states that can participate in charge transfer processes, thereby influencing the fluorescence behavior of the carbon dots. The peak at 287.58 eV is attributed to C═O groups in carboxyl or keto structures. Due to their strong electron-withdrawing ability, these groups can form electrostatic or weak coordination complexes with Hg^{2+}, promoting fluorescence quenching. The high-resolution N1s spectrum (Fig. 3(b)) reveals three types of nitrogen-doped sites: 398.55 eV (C═N–C, pyridinic nitrogen),

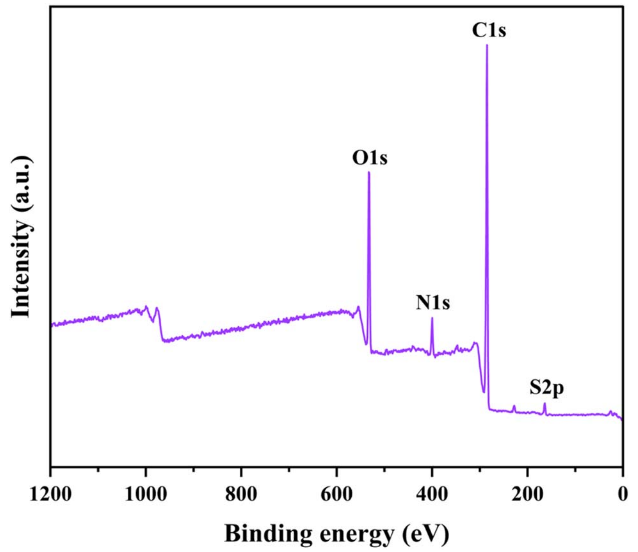

Fig. 2 Full XPS spectrum of N,S-CQDs.

399.76 eV ($N(C)_3$, graphitic nitrogen), and 401.53 eV (N–H, amino group).[32,33] These sites enhance the electron density and luminescence of the carbon dots and provide multiple active centers for the coordination and recognition of Hg^{2+}. In the high-resolution O1s spectrum (Fig. 3(c)), the peaks at 530.19 eV and 532.38 eV are assigned to C–O and C=O functional groups, respectively. These hydroxyl and carboxyl groups enhance the water solubility and stability of the carbon dots. Additionally, they can serve as electron donors or ligand sites, facilitating the recognition of Hg^{2+} and promoting fluorescence quenching.[34] Finally, The high-resolution S 2p spectrum (Fig. 3(d)) was deconvoluted into three sulfur chemical states, each represented by a spin–orbit doublet. The S $2p_{3/2}$ components located at 163.60 eV, 165.13 eV, and 167.75 eV were assigned to C–S–C, C–S–H, and sulfur oxide species, respectively. During fitting, the binding energy separation between S $2p_{3/2}$ and S $2p_{1/2}$ was fixed at 1.18 eV, with an area ratio of 2 : 1 and identical peak widths. The C–S–C and C–S–H sulfur species provide abundant soft-base sulfur sites that can form strong Hg–S coordination bonds, serving as the primary recognition centers for Hg^{2+} and inducing fluorescence quenching through electron transfer. The sulfur oxide peak at 167.75 eV, while contributing less to Hg^{2+} binding, reflects the diversity and complexity of surface functional groups generated during synthesis or post-processing. This is further supported by FT-IR spectroscopy, which confirms the presence of amino, hydroxyl, amide, and carboxyl functional groups, as well as successful nitrogen and sulfur co-doping in the N,S-CQDs.

3.3 Preparation and condition optimization of N,S-CQDs

As schematically illustrated in Fig. 4, N,S-CQDs were synthesized from waste lemon peel powder and glutathione through a one-step solvothermal process in DMF. The obtained N,S-CQDs exhibit strong blue photoluminescence under 370 nm excitation, reflecting their intrinsic optical properties. Based on these intrinsic photophysical characteristics, the effects of synthesis parameters on fluorescence performance were subsequently investigated to optimize the preparation conditions.

Before evaluating the fluorescence response of N,S-CQDs toward Hg^{2+}, their basic optical properties were first investigated to establish a clear understanding of the intrinsic photophysical behavior of the material. In this study, key parameters in the synthesis and fluorescence detection of N,S-CQDs were systematically optimized to achieve excellent fluorescence performance and high-sensitivity detection. Firstly, reaction time had a significant effect on the fluorescence intensity of the carbon quantum dots. The results showed that fluorescence intensity gradually increased as the reaction time was extended, reaching a maximum at 10 hours. Beyond this point, the fluorescence intensity decreased significantly. This change may be related to further carbonization of the carbon dots or the loss of surface functional groups, which reduces their optical properties. Therefore, 10 hours was selected as the optimal reaction time. As shown in Fig. 5(b), the fluorescence intensity increased gradually with rising temperature, reaching a maximum at 180 °C. At higher temperatures, the fluorescence intensity decreased. These results indicate that an appropriately high temperature facilitates the formation of the carbon dot structure and the doping of heteroatoms, while excessively high temperatures promote over-carbonization and suppress fluorescence performance. Therefore, 180 °C was selected as the optimal synthesis temperature. The addition of GSH as a nitrogen and sulfur source also plays a key role in determining the fluorescence properties of the carbon dots. The results shown in Fig. 5(c) indicate that increasing the amount of GSH significantly enhanced the fluorescence intensity, reaching a maximum at 0.2 g. Further increases in GSH dosage resulted in a decrease in fluorescence intensity. It is hypothesized that a moderate amount of GSH promotes the formation of functional groups and enhances doping efficiency, while an excessive amount may introduce structural defects or impurity doping, thereby reducing luminescence efficiency. The results in Fig. 5(d) show that the fluorescence quenching ratio of N,S-CQDs by Hg^{2+} is highest at pH 7. This indicates that a neutral environment favors effective binding and electron transfer between the carbon dot surface and Hg^{2+}. Acidic or alkaline environments may damage the structure of the carbon dots or alter their surface states, thereby weakening their detection performance. For response time optimization, the results in Fig. 5(e) show that the peak fluorescence quenching ratio is achieved after 10 minutes of interaction between N,S-CQDs and Hg^{2+} ions. Further extension of the reaction time offers little additional improvement, indicating that the system enables rapid and efficient detection. The results in Fig. 5(f) further indicate that room temperature (25 °C) provides the optimal quenching effect for the system. A temperature that is too low may inhibit the reaction rate, while excessively high temperatures can compromise the structural stability of the carbon dots and hinder effective binding to Hg^{2+}.

In summary, systematic optimization established the following optimal synthesis and detection conditions for N,S-

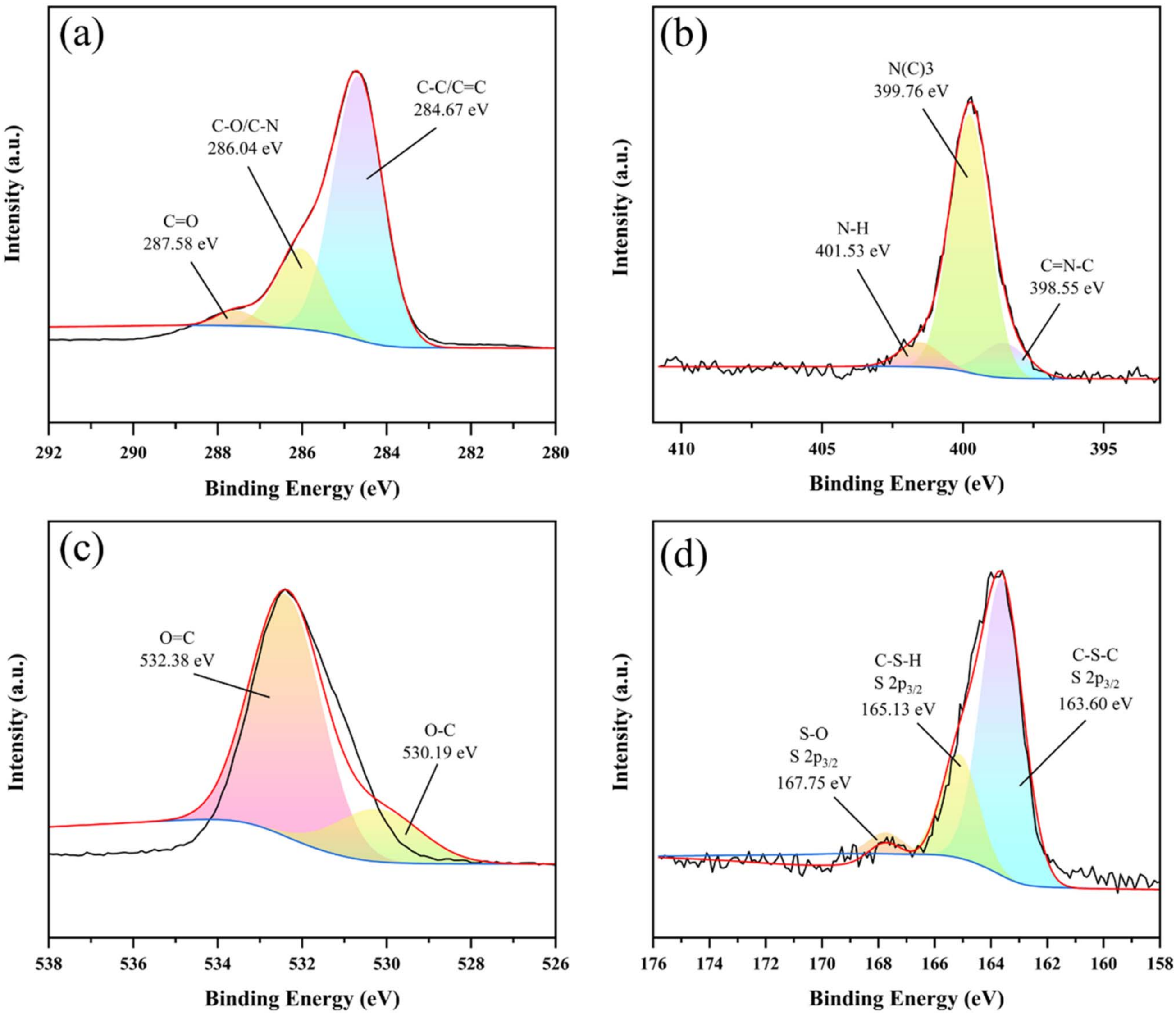

Fig. 3 (a–d) High-resolution XPS spectra corresponding to C1s, N1s, O1s, and S2p, respectively.

CQDs: reaction time of 10 hours, reaction temperature of 180 °C, and GSH addition of 0.2 g. The detection process was performed at pH 7 and 25 °C, with a reaction time of 10 minutes, enabling efficient detection of Hg^{2+}.

3.4 Selectivity and sensitivity for Hg^{2+} detection

Based on the optimized synthesis conditions and intrinsic optical properties discussed above, the selectivity and sensitivity of the N,S-CQDs toward Hg^{2+} were subsequently evaluated. As shown in Fig. 6(a), none of the other interferents, except for Hg^{2+}, caused significant changes in the fluorescence intensity. This indicates that the N,S-CQDs exhibit strong anti-interference performance in the presence of common metal ions and antibiotics. Among the tested ions, Cd^{2+} and Cu^{2+} caused some interference with Hg^{2+} detection, but the effect was limited. Most antibiotics did not significantly affect the fluorescence, while only levofloxacin, ampicillin, and ciprofloxacin caused slight fluorescence enhancement, which may be related to their intrinsic fluorescence properties. As shown in Fig. 6(b), the fluorescence decay curves of N,S-CQDs were fitted with an exponential function (red curve), yielding an average

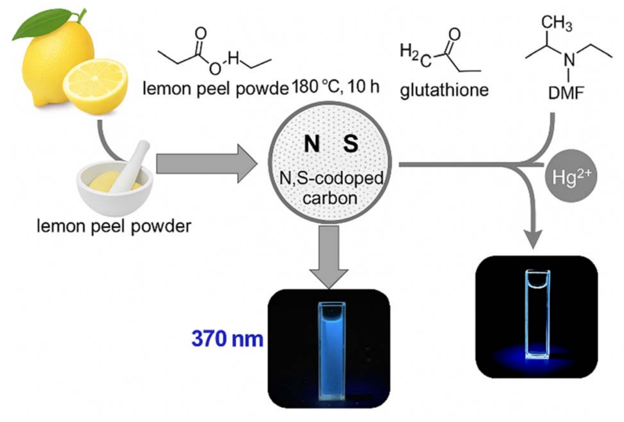

Fig. 4 Preparation of N,S-CQDs and detection of Hg^{2+}.

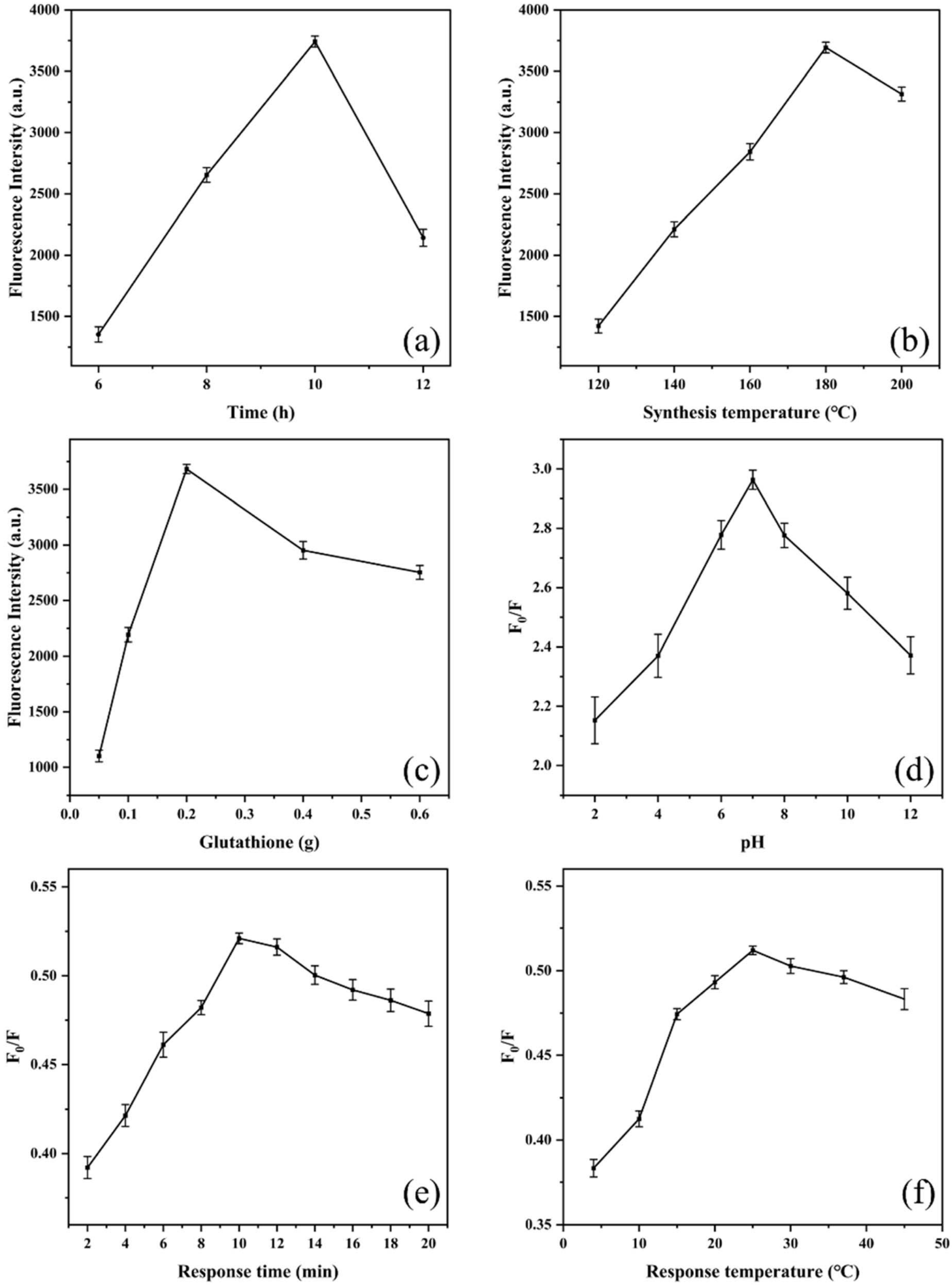

Fig. 5 (a) The fluorescence intensity of N,S-CQDs as a function of reaction time. (b) Fluorescence intensity of N,S-CQDs as a function of reaction temperature. (c) Fluorescence intensity of prepared N,S-CQDs as a function of GSH addition. (d) pH. (e) Fluorescence response time of N,S-CQDs upon addition of Hg^{2+}. (f) Effect of response temperature on the detection sensitivity of N,S-CQDs toward Hg^{2+}.

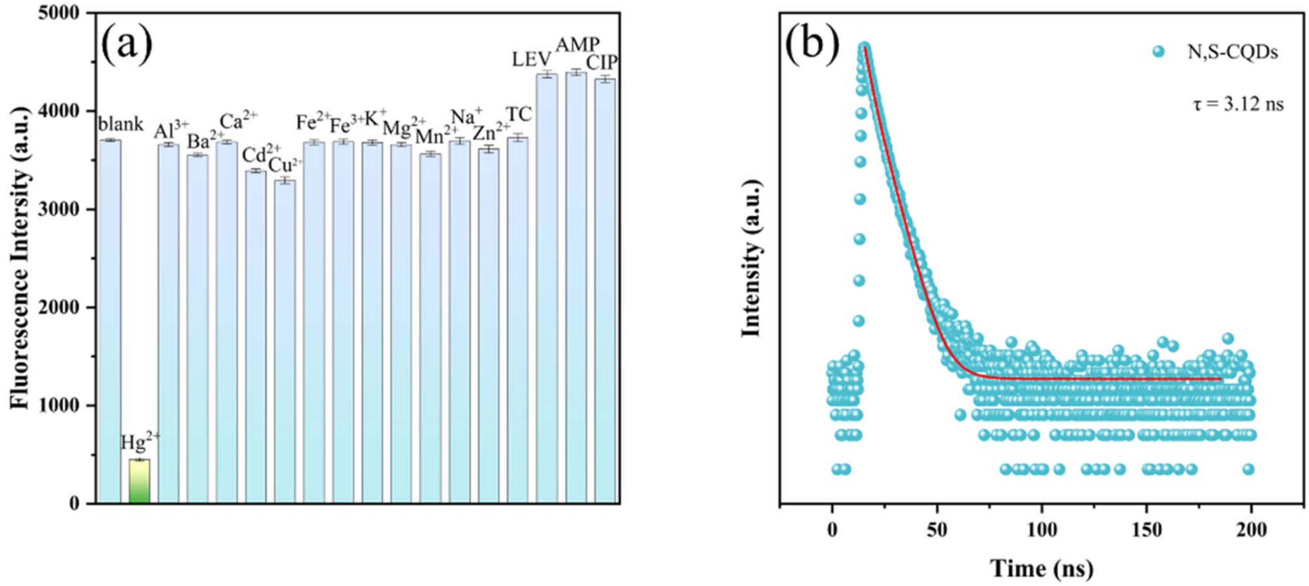

Fig. 6 (a) Effect of different metal ions and antibiotics on the fluorescence intensity of N,S-CQDs (Hg^{2+} concentration 1.0×10^4 nM, other interferents 6.0×10^4 nM, pH 7). (b) Fluorescence lifetime measurement of N,S-CQDs.

fluorescence lifetime (τ) of 3.12 ns. The lifetime value indicates good stability of the excited state and represents a typical nanosecond-scale fluorescence lifetime, consistent with the general characteristics of carbon quantum dot fluorescent materials.

In summary, the N,S-CQDs exhibited good selectivity and strong anti-interference ability for Hg^{2+}. Even at high concentrations of interfering agents, the probes were able to specifically recognize Hg^{2+}. These results demonstrate the potential of N,S-CQDs as fluorescent probes for Hg^{2+} detection in complex aqueous environments.

3.5 Detection of Hg^{2+} using N,S-CQDs fluorescent probes

Fig. 7(a) shows the three-dimensional fluorescence contour plot of N,S-CQDs. The maximum fluorescence intensity occurs at an excitation wavelength of 370 nm and an emission wavelength of 460 nm, indicating that the N,S-CQDs exhibit their strongest fluorescence response at these wavelengths. Fluorescence quenching is a phenomenon where a quencher molecule interacts with a fluorescent molecule, resulting in a decrease in the emission intensity of the fluorophore. As shown in Fig. 7(b), the N,S-CQDs exhibited a symmetric emission peak at 460 nm. Because N,S-CQDs have a strong affinity for Hg^{2+}, their fluorescence properties were systematically studied by gradually adding Hg^{2+} solutions under optimized conditions. The results showed that the fluorescence intensity of N,S-CQDs decreased significantly as the concentration of Hg^{2+} increased, accompanied by a slight blue shift in the emission band. This phenomenon can be attributed to the specific binding between the GSH surface capping layer and Hg^{2+}, which promotes electron or energy transfer and accelerates the fluorescence quenching mechanism.

To establish the relationship between the fluorescence intensity of N,S-CQDs and Hg^{2+} concentration, the Stern–Volmer equation[35] was applied as follows:

$$\frac{F_0}{F} = 1 + K_{SV}[Q] \tag{1}$$

where F_0 and F are the fluorescence intensities of N,S-CQDs in the absence and presence of Hg^{2+}, respectively; $[Q]$ is the concentration of Hg^{2+}; and K_{SV} is the Stern–Volmer constant. From eqn (1), two successive linear ranges were obtained: the first from 10 nM to 1000 nM ($R^2 = 0.9889$), and the second from 1 μM to 20 μM ($R^2 = 0.9882$), as shown in Fig. 7(c). The limit of detection (LOD) was calculated to be 17.6 nM using the 3σ method, indicating a low detection threshold. Therefore, the synthesized quantum dots are suitable for sensitive detection of Hg^{2+} even at nanomolar concentrations. The fluorescence quantum yield (QY) of the N,S-CQDs was determined by the relative method, using rhodamine B (QY = 95%, excitation at 370 nm) as the standard. Rhodamine B and N,S-CQDs were each dissolved in deionized water, and the absorbance was kept below 0.1 to avoid the internal filtration effect. Absorbance was measured using a UV-Vis spectrophotometer, and fluorescence emission spectra were recorded with a fluorescence spectrophotometer to calculate the integrated fluorescence area. The absorbance was plotted against the integrated fluorescence area using Origin software, as shown in Fig. 7(d), and the slope of the linear fit was determined. The fluorescence quantum yield (QY) of N,S-CQDs was calculated to be 15.2% according to eqn (2).[36,37]

$$\Phi_x = \Phi_{std} \times \left(\frac{K_x}{K_{std}}\right) \times \left(\frac{{\eta_x}^2}{{\eta_{std}}^2}\right) \tag{2}$$

In eqn (2), Φ_x and Φ_{std} represent the quantum yields of the sample and the standard, respectively. K is the slope of the linear fit between integrated fluorescence intensity and

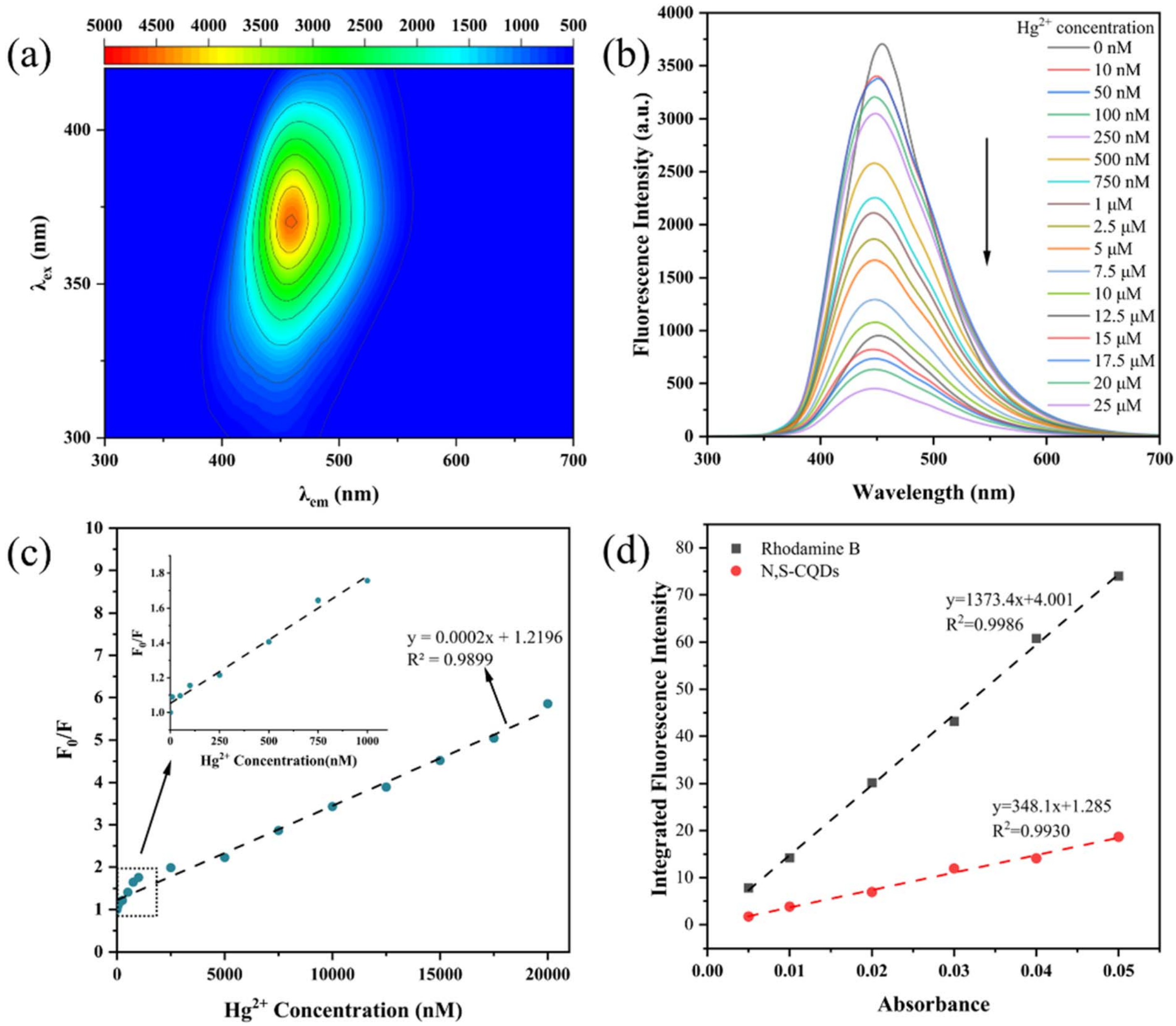

Fig. 7 (a) Fluorescence EEM spectra of N,S-CQDs. (b) Effect of Hg^{2+} concentration on fluorescence intensity of N,S-CQDs. (c) Relative fluorescence intensity of N,S-CQDs is linearly related to Hg^{2+} concentration. (d) Slope plots of rhodamine B and N,S-CQDs.

absorbance, and η is the refractive index of the solvent. The results indicate that the N,S-CQDs prepared in this study have a high fluorescence quantum yield and show superior performance compared to similar carbon quantum dots.

3.6 Detection of Hg^{2+} in real water samples

To evaluate the reliability of the proposed sensor in complex water matrices, standard validation parameters, including recovery, relative standard deviation (RSD), and repeatability, were systematically assessed. The lake water samples were centrifuged at 8000 rpm for 10 minutes and then purified by filtration through a 0.22 μm membrane. Different concentrations of standard Hg^{2+} solutions were added to the water samples for analysis. As shown in Table 1, the recoveries of Hg^{2+} in lake water ranged from 98.5% to 101.8%, with relative standard deviations (RSDs) between 0.48% and 3.25%, all below 5%. The results demonstrate that this method has high accuracy and precision, and is suitable for the determination of Hg^{2+} in lake water samples.

Table 2 compares the performance of the N,S-CQDs synthesized in this study with various carbon quantum dots reported in the literature for Hg^{2+} detection. N-CDs (LOD: 0.10 μM), Au/N-CQDs (0.118 μM), Mg–N-CQDs (0.02 μM), single N-CDs (0.02 μM), CDs/MSNs (0.89 μM), and N/S-CDs (0.32 μM) were mostly detected within a linear range of 0–25 μM or broader. In contrast, the N,S-CQDs prepared in this work achieved a wide linear range of 0–25 μM and a detection limit for Hg^{2+} as low as 0.0176 μM in lake water samples. This detection limit is about

Table 1 Recoveries after standard addition using the method developed in this study

Sample	Spiked/nM	Found/nM	Recovery %	RSD %
Sample 1	50	49.25 ± 1.60	98.50 ± 3.20	3.25
Sample 2	100	101.78 ± 2.54	101.78 ± 2.54	2.50
Sample 3	500	495.12 ± 8.92	99.02 ± 1.78	1.80
Sample 4	1000	998.34 ± 14.97	99.83 ± 1.50	1.50
Sample 5	5000	4967.23 ± 23.81	99.34 ± 0.48	0.48

Table 2 Comparison of the performance of N,S-CQDs prepared in this study with previously reported fluorescent sensors for Hg^{2+} detection

Carbon dots	Linear range (μM)	LOD (μM)	Sample types	Sample types
N-CDs	3 ∼ 100	0.1	Chinese traditional herb	38
Au/N-CQDs	0 ∼ 41.86	0.118	Water	39
Mg–N-CQDs	0 ∼ 25	0.02	River water	40
N-CDs	0 ∼ 24	0.02	Water	41
CDs/MSNs	0 ∼ 10 000	0.89	Lake water	42
N/S-CDs	0.2 ∼ 20	0.32	Water	43
N,S-CQDs	0 ∼ 25	0.0176	Lake water	This study

12% lower than the previous best report (0.02 μM), reaching a leading level for trace Hg^{2+} detection in lake water.

3.7 Possible mechanism of Hg^{2+} induced fluorescence quenching

The fluorescence quenching of N,S-CQDs by Hg^{2+} is mainly attributed to the specific interactions between surface ligands and Hg^{2+}, which modulate the energy level structure of the quantum dots. At lower concentrations, Hg^{2+} initially bind to the sulfhydryl groups in GSH molecules, leading to partial desorption or rearrangement of surface ligands.[44] This process increases the number of surface defects on the carbon quantum dots, resulting in decreased fluorescence intensity and a concurrent blueshift of the emission peak.[45] As the concentration of Hg^{2+} increases, Hg^{2+} reacts with sulfur atoms on the surface of the quantum dots to form HgS nanoparticles *in situ*.[46] This process significantly alters the surface energy level structure and promotes non-radiative recombination of electrons and holes, resulting in more pronounced fluorescence quenching. The Stern–Volmer quenching curves displayed two distinct linear regions, further indicating that the quenching process is concentration-dependent and involves multiple phases. Overall, the fluorescence quenching in this system is primarily governed by surface state modulation and electron transfer mechanisms, while internal filtering effects play a relatively minor role.

4 Conclusions

In this study, nitrogen and sulfur co-doped carbon quantum dots (N,S-CQDs) were successfully synthesized *via* a one-pot hydrothermal route in DMF, employing waste lemon peel as a sustainable carbon source and reduced glutathione as the N,S co-dopant. The optimized N,S-CQDs exhibited a uniform particle size of approximately 2.45 nm and a fluorescence quantum yield of 15.2%. Owing to their strong blue emission and efficient surface functionalization, a highly sensitive and selective fluorescence quenching assay for Hg^{2+} detection was established. The probe displayed a linear response in the concentration range of 17.6 nM–20 μM with a remarkably low detection limit of 17.6 nM. When applied to real lake water samples, the method achieved satisfactory recoveries (98.5–101.8%) and low relative standard deviations (0.48–3.25%), confirming its reliability for practical analysis. Overall, the as-developed N,S-CQDs-based fluorescent sensor combines a facile synthesis route with rapid response, good stability, and high sensitivity, providing a promising and sustainable analytical platform for Hg^{2+} monitoring in environmental water samples. This study advances CQD-based Hg^{2+} sensing by rationally tailoring surface chemistry and demonstrating reliable performance in real water matrices.

Author contributions

Yongjian Pan: conceptualization, data curation, formal analysis, methodology, validation, writing – original draft, writing – review & editing. Shancai Guo: conceptualization, formal analysis, data curation, software. Teng Wang: investigation, data curation. Jianyuan Lin: writing – review & editing, funding acquisition, methodology, validation. Zhijian Jia: investigation, formal analysis, funding acquisition, project administration, resources. Fuhang Xu: investigation, data curation, funding acquisition, writing – review & editing. Renyue Huang: formal analysis, investigation, data curation, visualization. Haili Wang: writing – review & editing, validation, supervision, project administration. Chunjie Bai: supervision, resources. Jinghua Chen: supervision, resources.

Conflicts of interest

There are no conflicts to declare.

Data availability

The data that support the findings of this study are available from the corresponding authors upon reasonable request.

Acknowledgements

This research was supported by Zhejiang Provincial Top Key Discipline of Biological Engineering (Level A) (No. KF2025004, No. KF2024003, No. CX2024010, No. CX2024058, No. CX2025007, No. CX2025018); A graducation reform project of the 14th five year plan in Zhejiang province of modern instrumental analysis technology(No. 20231); This Research was Supported by General Research Project of the Education of Zhejiang Province (No. Y202456565); Zhejiang Provincial Level Innovation and Entrepreneurship Training Program for College Students (No. S202410876085, No. S202310876023); The Key Laboratory of Quality and Safety Testing and Control of Ningbo Characteristic Agricultural Products (No. KF202309); Research on Feedforward Control Mechanisms for Preventing Major Food Safety Incidents (ZYH2015005).

References

1 H. Li, Z. Yang, W. Zheng, L. Leng, J. Yang, W. Qu and H. Li, *Sep. Purif. Technol.*, 2025, **363**, 131917.
2 Z. Liu, J. Zhou, L. Zhou, B. Li, T. Wang and H. Liu, *Sep. Purif. Technol.*, 2024, **337**, 126352.
3 X. Feng, P. Li, X. Fu, X. Wang, H. Zhang and C.-J. Lin, *Environ. Sci. Process. Impacts*, 2022, **24**, 634–648.
4 M. Guo, J. Du, H. Li, Y. Lei, J. Liu, H. Lu, C. Yan and H. Hong, *Ecol. Indic.*, 2025, **176**, 113707.
5 M. E. Robles, Y. Oh, M. T. Haque, M. Jeon and L.-H. Kim, *Appl. Sci.*, 2025, **15**, 6502.
6 Z. Li, Y. Tong, Z. Wu, B. Liao, G. Liu, L. Xia, C. Liu and L. Zhao, *J. Hazard. Mater.*, 2025, **491**, 138009.
7 M. M. Al-Sulaiti, L. Soubra and M. A. Al-Ghouti, *Curr. Pollut. Rep.*, 2022, **8**, 249–272.
8 C. Hui, B. Ma, S. Hu and C. Wu, *Environ. Pollut.*, 2024, **341**, 123016.
9 Z. Gojkovic, S. Simansky, A. Sanabria, I. Marova, I. Garbayo and C. Vilchez, *Microorganisms*, 2023, **11**, 2034.
10 C. O. R. Okpala, G. Sardo, S. Vitale, G. Bono and A. Arukwe, *Crit. Rev. Food Sci. Nutr.*, 2018, **58**, 1986–2001.
11 P. Coufalík, O. Zvěřina, K. Sádovská and J. Komárek, *J. Food Compos. Anal.*, 2023, **124**, 105668.
12 K. A. Romanovskiy, M. A. Bolshov, A. V. Münz, Z. A. Temerdashev, M. Yu. Burylin and K. A. Sirota, *Talanta*, 2018, **187**, 370–378.
13 F. Li, P. Zhang, J. Chen, J. Xi, S. Gao and Y. Liu, *Microchem. J.*, 2025, **213**, 113883.
14 A. K. Das, M. S. Saikh, A. Misra, M. S. Ali, P. Pradhan, N. Sepay, S. Dhibar, M. Afzal, S. J. Abbas and N. Sepay, *J. Mol. Struct.*, 2026, **1352**, 144012.
15 Green Synthesized Biogenic Ag Nanoparticles With Enhanced Antibacterial, Antifungal, Antibiofilm, and Antioxidant Activities: Catalytic Applications in the ipso-Hydroxylation of Aryl Boronic Acids - Das, *Applied Organometallic Chemistry*, Wiley Online Library, 2025, https://onlinelibrary.wiley.com/doi/10.1002/aoc.7796, accessed December 18, 2025.
16 A. K. Das, A. Misra, M. S. Ali, M. S. Saikh, S. Dhibar, K. K. Banerjee, G. Ghatak, D. Mal, M. Shit and S. Biswas, *RSC Adv.*, 2025, **15**, 35844–35858.
17 A. K. Das and K. Sarkar, *New J. Chem.*, 2025, **49**, 12898–12930.
18 A. Ghatak, A. Pramanik, A. K. Das and S. Bhar, *Tetrahedron*, 2022, **127**, 133090.
19 Z. Wang, J. Zhao, T. Mani, Y. Tai, T. Liang, J. Nam, Y. Yin, Dual Doping and Porous Fluoropolymer Integration of ZnS for Enhanced Mechanoluminescence with Concurrent Photoluminescence and Afterglow, *Advanced Functional Materials*, Wiley Online Library, https://advanced.onlinelibrary.wiley.com/doi/abs/10.1002/adfm.202517279, accessed December 18, 2025.
20 H. Li, Z. Chen, Z. Chen, Q. Qiu, Y. Zhang, S. Chen and Z. Wang, *Chin. J. Org. Chem.*, 2023, **43**, 3067–3077.
21 S. Wahyudi, J. Abdul Aziz, F. Faizal and A. Bahtiar, *Results Mater.*, 2024, **21**, 100551.
22 O. A. Aladesuyi and O. S. Oluwafemi, *Inorg. Chem. Commun.*, 2023, **153**, 110843.
23 H. Qi, X. Sun, T. Jing, J. Li and J. Li, *RSC Adv.*, 2022, **12**, 1989–1997.
24 L. Dewangan, Y. Chawre, J. Korram, I. Karbhal, R. Nagwanshi, V. Jain and M. L. Satnami, *Microchem. J.*, 2022, **182**, 107867.
25 M. B. Cánchig, F. López, Z. Morales-Navarro, A. Debut, K. Vizuete, T. Terencio, M. Caetano and J. P. Saucedo-Vázquez, *Carbon Trends*, 2025, **18**, 100445.
26 G. Alba, M. Pilar Villar, R. Alcantara, J. Navas and D. Araujo, *Nanomaterials*, 2020, **10**, 1193.
27 Y. Wang, S. Yao, H. Zheng, Z. Zuo and Y. Liu, *Int. J. Coal Geol.*, 2025, **301**, 104714.
28 O. A. Aladesuyi and O. S. Oluwafemi, *Appl. Water Sci.*, 2024, **14**, 153.
29 E. Binaeian and S. Rohani, *Appl. Mater. Today*, 2025, **44**, 102782.
30 A. H. Rizvi, R. Fatima, A. Ahmad and M. A. Aziz, *Microchem. J.*, 2025, **208**, 112537.
31 Y. Liu, H. Ren, Z. Gong, B. Tan, W. Lan, Q. Dai, X. Zheng, L. Guo, A. A. AlObaid and I. Warad, *J. Ind. Eng. Chem.*, 2024, **137**, 593–605.
32 Y. Venkatesh, S. Wadepalli, P. R. Bangal, P. V. S. Naidu and P. A. Rao, *Luminescence*, 2025, **40**, e70108.
33 M. Chaghazardi, S. Kashanian, M. Nazari, K. Omidfar, Y. Joseph and P. Rahimi, *Photonics*, 2024, **11**, 841.
34 B. S. Gómez Pineros and G. Granados-Oliveros, *J. Mol. Struct.*, 2024, **1317**, 138990.
35 H. Kumar, J. Duhan and S. Obrai, *J. Mol. Struct.*, 2024, **1309**, 138046.
36 H. Yu, X. Li, P. Yin, S. Fang, J. Ma, Y. He, W. Yang, W. Tan and S. Li, *Process Saf. Environ. Prot.*, 2025, **200**, 107423.
37 C. Wang, Y. Wang, H. Shi, Y. Yan, E. Liu, X. Hu and J. Fan, *Mater. Chem. Phys.*, 2019, **232**, 145–151.
38 L. Wu, H. Liu, T. Liu and C. Li, Nitrogen-doped Carbon Dots: Application of Hg Ions Detection in Rannasangpei, *Chem. Res. Chin. Univ.*, 2019, **35**(4), 577–580.
39 A. Meng, Q. Xu, K. Zhao, Z. Li, J. Liang and Q. Li, *Sens. Actuators, B*, 2018, **255**, 657–665.
40 T. Liu, N. Li, J. X. Dong, H. Q. Luo and N. B. Li, *Sens. Actuators, B*, 2016, **231**, 147–153.
41 A. Iqbal, K. Iqbal, L. Xu, B. Li, D. Gong, X. Liu, Y. Guo, W. Liu, W. Qin and H. Guo, *Sens. Actuators, B*, 2018, **255**, 1130–1138.
42 X. Miao, J. Liu, H. Li, C. Tao, Y. Zhang and X. Yang, *Diam. Relat. Mater.*, 2024, **148**, 111434.
43 D. Sun, T. Liu, C. Wang, L. Yang, S. Yang and K. Zhuo, *Spectrochim. Acta, Part A*, 2020, **240**, 118598.
44 W. Zhao, R. Zhai, Q. Chen, C. Huang, H. Li, Y. Zhu, Y. Duan and J. Gao, *Anal. Methods*, 2024, **16**, 4951–4959.
45 J. Feng, L. Shi, D. Chang, C. Dong and S. Shuang, *Chem. Eng. J.*, 2024, **490**, 151839.
46 N. Khoa Hien, T. T. G. Chau, N. Dinh Luyen, Q. V. Vo, M. V. Bay, S. Tung Ngo, P. Cam Nam and D. Tuan Quang, *RSC Adv.*, 2025, **15**, 20125–20133.

